# EXHIBIT H

The International Journal of

# Robotics Research

Volume 9, Number 3, June 1990
ISSN 0278-3649
Published by The MIT Press

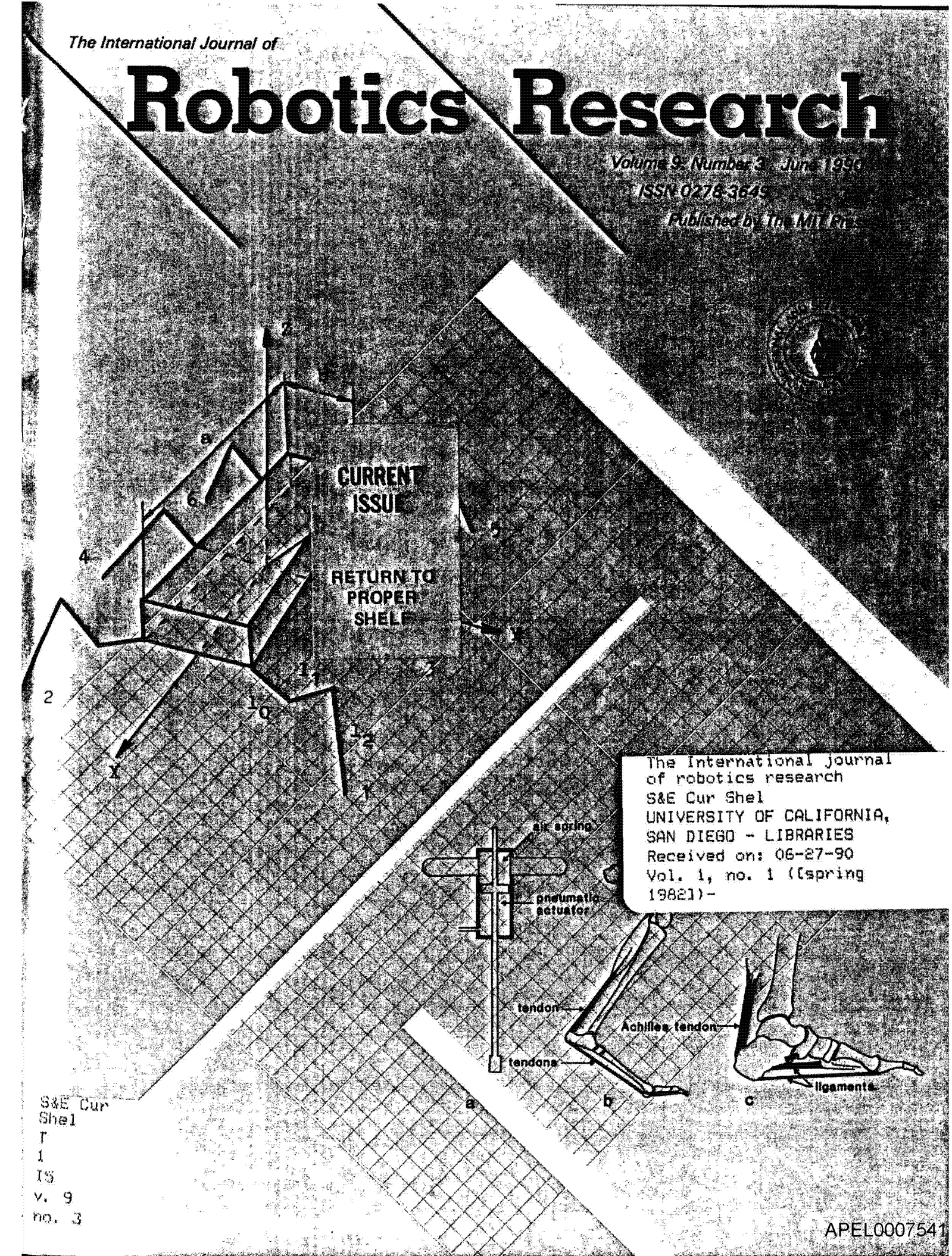

**The International Journal of Robotics Research** (ISSN 0278-3649) is a bimonthly review published February, April, June, August, October, and December by the MIT Press, Cambridge, Massachusetts, and London, England.

**Business Offices:** Subscriptions, address changes, and mailing list correspondence should be addressed to Journals Department, The MIT Press, 55 Hayward Street, Cambridge, MA 02142.

**Subscription Rates:** $70.00 for individuals and $140.00 for institutions. Subscribers outside the United States and Canada add $17.00 for surface postage, $28.00 for airmail. Single copies of current issues: $25.00. To be honored free, claims for missing issues must be made immediately upon receipt of the next published issue. Circulation Department (617) 253-2889.



**Postmaster:** Send address changes to *The International Journal of Robotics Research,* 55 Hayward Street, Cambridge, MA 02142. Second class postage paid at Boston and at additional post offices.

**Advertising:** Advertising Manager, The MIT Press Journals Department, 55 Hayward Street, Cambridge, MA 02142 (617) 253-2866.

*The International Journal of*
# Robotics Research
Volume 9, Number 3, June 1990

## Contents

**R. S. Fearing**
Department of Electrical Engineering and Computer Science
University of California
Berkeley, California 94720

# Tactile Sensing Mechanisms

## Abstract

*This paper has three main themes: design of a cylindrical tactile sensor, mechanical analysis using planar linear elasticity models, and signal analysis for determining basic information about the applied contact. An analysis of appropriate sensor depth has been used to allow accurate localization of contacts and reduced spatial aliasing. A comparison has been made between the cylindrical sensor and a simple two-dimensional stress-strain model. The effects of skin thickness and sensor depth on sensitivity are analyzed. Preliminary methods for determining contact location, total force, and tangential force with only normal deflection sensors have been implemented for a line contact.*

## 1. Introduction

Local contact information from the fingers is important for dextrous manipulation with multifingered hands. Experiments with open-loop finger force control for a dextrous hand have shown the need to determine contact types and location at the finger tips (Fearing 1986). Some of the most useful parameters to recover are angle and magnitude of force, surface normals, location of contact, curvature, and type of contact (point, line, plane); see for example, Fearing (1984). It is necessary to know the location of the contact on the finger for accurate force application. This article addresses tactile finger design issues, the transduction mechanism, and determination of contact location and magnitude using linear filtering techniques. A paper (Fearing and Binford 1988), based on Fearing (1987b), discusses using nonlinear model-based inverse filtering to recover surface curvature and orientation from a static set of strain measurements. Transduction and inversion methods are also discussed in Cameron et al. (1988) and Speeter (1987).

Two different approaches to obtaining contact information are: a finger-tip sensor that gives location and resultant force using a strain gauge structure (Brock and Chiu 1985; Bicchi and Dario 1987) and one that uses arrays of deflection transducers (Hillis 1981; Boie 1984; Chun and Wise 1985; Siegel et al. 1985). The array sensor approach has an advantage for determining contact shape from a single measurement.

In one sense, $N \times M$ measurements with a single element tactile sensor can be equivalent to one measurement at each of $N \times M$ sensors. However, objects move while being manipulated with the fingers. Object motion makes it nice to have simultaneous measurement over the whole finger surface. It is difficult and time consuming to explore the object using single tactile sensors to determine contact type if the object must remain grasped. In addition, multiple contacts where the fingers touch each other as well as the object are quite common and can fool a sensor that gives only the resultant force at a single point. Strain gauges are good for measuring quantities of force, but an array sensor is better for describing surfaces.

Flat sensors are not very useful for manipulation with dextrous hands. Round shapes are better for rolling objects about fingers (Fearing 1986). A tactile sensor array was packaged in a molded rubber finger tip for the Stanford/JPL hand as shown in Figure 1. There are $7 \times 12$ tactile elements (tactels) on the cylindrical portion and $1 \times 12$ elements underneath the hemispherical tip for a total of $8 \times 12$ capacitive sensing elements. Only an $8 \times 8$ subset ($7 \times 8$ on cylinder and $1 \times 8$ under the tip) is externally connected to the interface electronics. The sensor density has been increased from previously reported work (Fearing 1987a) to reduce aliasing and is now adequate for local contact determination. Other cylindrical finger tips are a 133-element device described in Allen and Bajczy (1985) and a 256-element fiber-optic device (Begej 1988). The main goal is the use of this finger as an ex-

The International Journal of Robotics Research,
Vol. 9, No. 3, June 1990,

*Fig. 1. Tactile sensing finger for Stanford/JPL hand.*

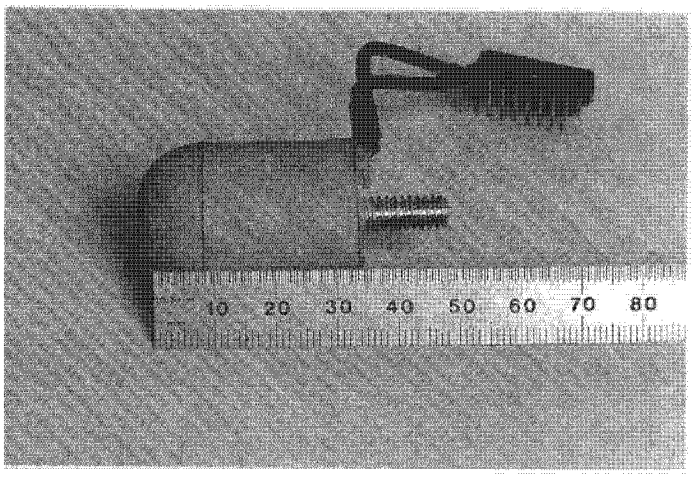


*Fig. 2. Capacitive sensor block diagram.*

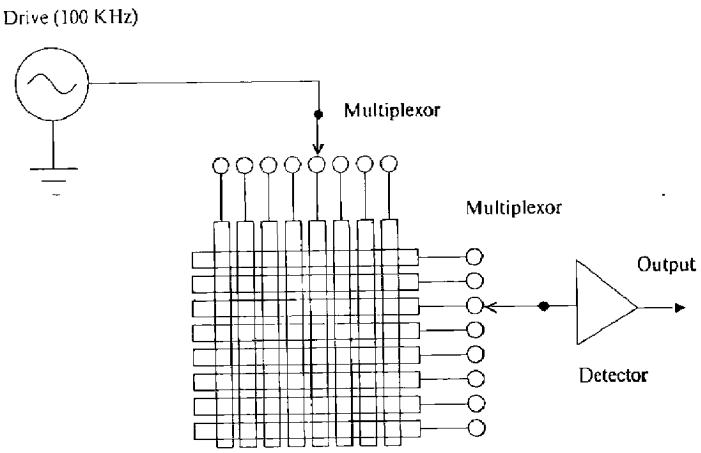


perimental device for sensory and manipulation research. The finger is not intended as a final prototype and is probably not robust enough for industrial use. It is, however, rather sensitive and reasonably durable in laboratory use.

## 2. Finger Construction/Design Criteria

The primary criteria used in designing the tactile finger tip were good sensitivity and low aliasing as described by Fearing and Hollerbach (1985), and ease of fabrication so that many designs could be quickly evaluated. These considerations and the success of other workers with capacitor arrays (Siegel et al. 1985; Boie 1984; Boie and Miller 1985) led us to build tactile arrays from capacitors. However, the sensor analysis developed here is for the most part independent of the transduction mechanism used.

### 2.1. Electrical Design

As shown in Figure 2, capacitors are formed at the intersection of rows and columns of conductive strips. As in the method used by Siegel (1986), the capacitance at a junction is measured by the amplitude of the output voltage for a selected row and column. Unused rows and columns are switched to ground potential to improve shielding and reduce cross-talk. The $8 \times 8$ array was originally scanned at 15 Hz, but the rate was reduced to 7 Hz for improved noise performance. This low scanning speed could be increased, but since the analysis has been done for static forces only, it has not been a limitation.

Simplicity of construction was an issue; thus the electronics are mounted remotely from the sensor at the base of the hand, at a distance of about 30 cm. While performance would be significantly improved by having the electronics built into the finger tip, it was not felt that the sensor design was stable enough for the considerable cost of installing electronics internally. A significant fraction of the signal is thus lost in the shielding capacitance. The large capacitance of this sensor allows significant cable capacitance. Two shielded cables are required to reduce coupling, one for driving the array and one for sensing the array output. Improvements in sensitivity and reduced wiring constraints could be accomplished by a custom hybrid circuit embedded in the core of the finger.

### 2.2. Measurement

Using an amplifier with input impedance $R_L$, the voltage output of the tactile sensor $V_s$ is given by

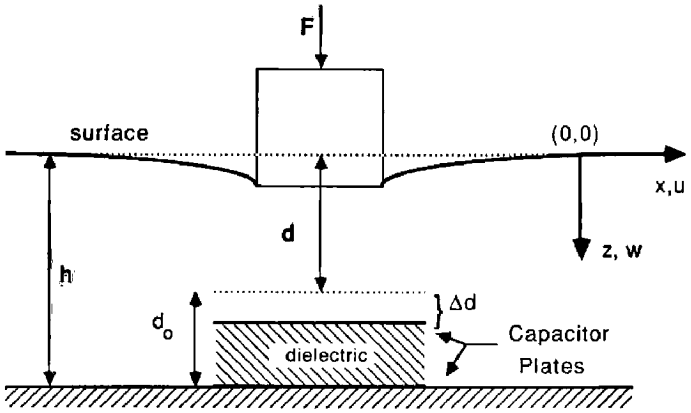


*Fig. 3. Capacitor in elastic strip model.*

$$|V_S| = \frac{C_S R_L \omega}{\sqrt{1 + [\omega R_L (C_S + C_L)]^2}} |V_d| \approx \frac{C_S R_L \omega}{\omega R_L C_L} |V_d| = \frac{C_S}{C_L} |V_d|, \quad (1)$$

where $V_d$ is the drive voltage and $C_S$ is the sensor capacitance at one junction. The effects of stray capacitances between unselected rows and columns, cable capacitance, and amplifier input capacitance are lumped into the load capacitance $C_L$. The capacitances for the unselected rows and columns will change with pressure; thus the cable capacitance should be made to dominate. With the cable capacitance from the sensor to the amplifier and the amplifier input capacitance significantly larger than the sensor capacitance ($C_L \gg C_S$) and sufficiently large frequency $\omega$, the approximation in eq. (1) is valid.

Figure 3 shows a simple capacitor model that assumes capacitor plate compression without twisting. The formula for the sensor capacitance (valid for thin plates) is:

$$C_S = K_o \epsilon_o \frac{A}{d_o - \Delta d} \quad (2)$$

where $K_o$ is the dielectric constant, $\epsilon_o$ is the permittivity of free space, $A$ is the plate area, $d_o$ is nominal plate separation, and $\Delta d$ is the plate displacement. The actual capacitance may be larger as a result of fringing fields, because the plate area is not very large compared to the separation $d$. The sensor has conductors of width 2.5 mm and 5.1 mm and separation of 0.5 mm. The capacitance is about 1 pF for the dielectric constant of about 4.

From the arguments given in Fearing and Hollerbach (1985), the normal strain beneath the surface is an important quantity to measure. To approximate measuring the subsurface strain $\epsilon_z$, we use

$$\frac{\Delta d}{d_o} \approx \epsilon_z, \quad (3)$$

where $\Delta d$ is the displacement of the top plate of the capacitor, $d_o$ is small, and $\Delta d \ll d_o$. Ignoring tilting of plates (parallel translation of the plates has no effect since the bottom plate is very long), the percent deflection signal is obtained by:

$$\frac{V_S - V_o}{V_S} = \frac{\frac{C_S}{C_L} - \frac{C_{So}}{C_L}}{\frac{C_S}{C_L}} = 1 - \frac{\frac{1}{d_o}}{\frac{1}{d_o - \Delta d}} = \frac{\Delta d}{d_o}, \quad (4)$$

where $C_{So}$ is the nominal undeflected capacitance. This ratio of voltage measurements is a well-behaved function.

Since it can be assumed that $V_S$ and $V_o$ for each particular cell are measured with the same wiring and amplifier and the same $A$, $\omega$, $R_L$, and $C_L$ parameters, the fractional deflection is independent of these constant parameters. The fractional deflection for a particular cell and given force depends to first order only on the modulus of elasticity for that cell, if all cells are at the same depth. Percent deflection will be used as a first-order approximation to strain throughout this paper and compared directly to the normal strain.

### 2.3. Mechanical Design

The finger size and shape are chosen for good grasping. Curved surfaces are needed for rolling objects about the fingers (Fearing 1986). In these operations, contact can occur anywhere on the finger, not just on the palmar surface; thus complete sensor coverage of the finger is necessary. The finger tip is made of a cylin-

*Fig. 4. Finger tip construction.*

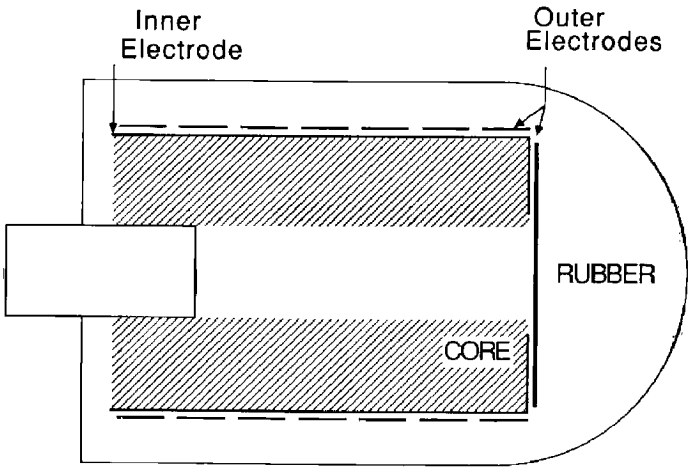


drical section 25 mm long and 25.4 mm in diameter, with a hemisphere at the end. The goal of complete coverage with a $7 \times 8$ array on the cylinder led to 3.8 mm center-to-center spacing along the length and 45° spacing around the circumference for the initial design. For improved spatial performance, the latest versions use 3.3 mm spacing along the length and 18° spacing around the circumference.

The free design parameter is the sensor depth. From Fearing and Hollerbach (1985), the sensor depth should be twice the sensor spacing for negligible aliasing from sampling of the continuous subsurface strain response. But a good signal-to-noise ratio (that is, good sensitivity) is also needed. The strain is inversely proportional to depth. As a compromise between sensitivity and aliasing, the sensor depth was chosen approximately equal to the sensor spacing.

The overall finger tip structure is shown in Figure 4. A lightweight Delrin core, 17.7 mm in diameter, provides structural integrity. In the newest design, the driven electrodes are the seven outer "rings" of 2.5 mm width copper spaced at 3.3 mm and a disc connected as the eighth ring to give sensory coverage at the tip. The rings are separated from the strips by a compliant dielectric of about 0.5 mm thickness, which is a molded open-cell rubber layer. For force transmission and protection, the finger covering is molded with DPR 4280-LV (Hardman Inc.) rubber. This rubber was chosen for its very low tensile modulus, which is measured to be about $2.5 \times 10^5$ Nm$^{-2}$. The rubber is incompressible, as Poisson's ratio, $\nu \approx 0.5$, was verified experimentally on a separate sample.

*Fig. 5. Structure of molded dielectric layer.*

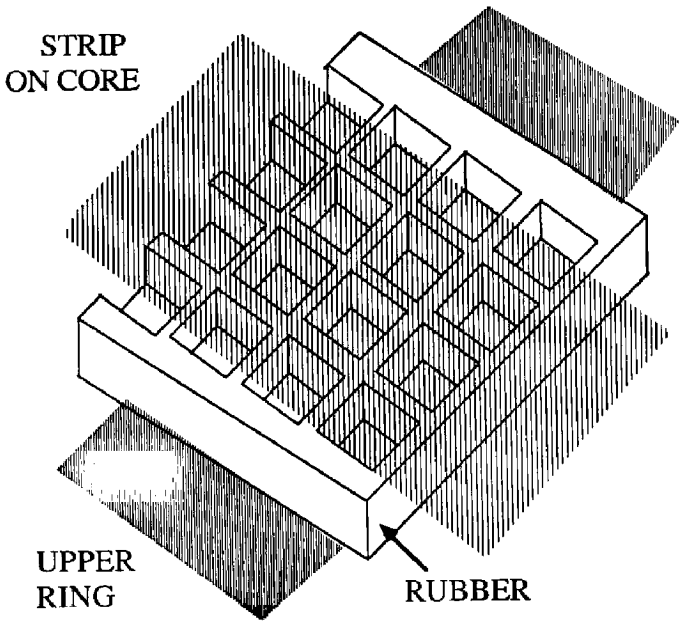


For increased sensitivity, a foam dielectric layer much softer than the surrounding rubber was initially used (measured at $7 \times 10^4$ Nm$^{-2}$ modulus). The softer dielectric also helps to widen the sensor response because of the tendency for the harder rubber to move as a whole layer without deforming. In the limiting case of a rigid plate on an elastic foundation, the spatial impulse response is as wide as the entire sensor. The skin depth can be reduced because of the wider impulse response to obtain improved sensitivity without increasing aliasing. (See section 6 for discussion of aliasing issues.)

The foam absorbed rubber during molding in some places, decreasing the sensitivity of some cells. Thus the dielectric was changed from soft foam to a structure molded from the same rubber as the skin layer for increased strength and homogeneity (Fig. 5). This structure includes hollow spaces to give it some of the same sensitivity as the foam. A test finger with a solid rubber dielectric of about 0.7 mm thickness had only about one-fourth the sensitivity of the molded dielectric. Siegel et al. (1985) and Siegel (1986) describe using tabs in the dielectric layer to increase compressibility.

Unwrapped, the linear separation of the elements around the circumference for 45° spacing is about 8 mm, which would cause a lot of aliasing. Since the

*Fig. 6. Percent deflection vs. applied load to one cell.*

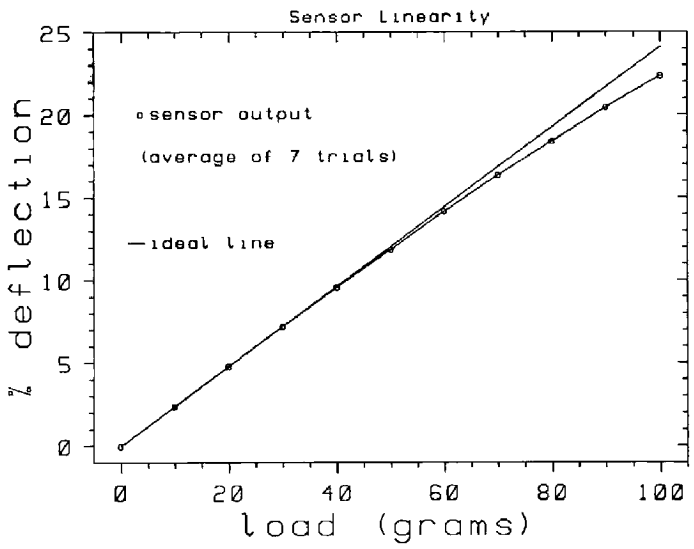


copper is orders of magnitude stiffer than the rubber, it does not stretch, but can only bend, approximately like a beam. This beam-like property of the rings gives the sensor much better overlap and reduces aliasing around the circumference to a greater degree than might be obtained with a compliant conductor. The rings are on the outside for improved resolution along the length of the finger, which is more important than localization around the circumference for manipulation (Fearing 1986).

## 3. Performance Evaluation

An important parameter for evaluating a tactile sensor is the sensitivity of each tactile element (tactel). The least sensitive cells in the finger array give 6% deflection for a 50-gram weight on a 7.8-mm$^2$ area probe (a 3.2-mm diameter hemisphere). A 50-gram load on a cell with an undeflected voltage output ($V_o$) of 2000 A/D units gives seven bits of signal for a 6% deflection. The pressure sensitivity of this cell is 0.06 gm mm$^{-2}$ for a sensed voltage ($V_S$) change of 1 A/D unit. The pressure sensitivity figure of 0.06 gm mm$^{-2}$ has little meaning, because the response is also a function of the pressure distribution. The real figure of merit is a force sensitivity of about 0.5 gm ($\approx$ 100 A/D units for 50-gm load) specified with this particular probe. As described in Fearing and Hollerbach (1985), the measured strain is a function of the spatial frequencies of the applied pressure. The same force applied to a larger contact area can give a larger peak strain. An approximate method for determining the load from the strain for varying contact sizes is described in section 8.

Figure 6 shows the monotonic response of one cell to increasing weight as determined from the capacitor sensor voltage output using eq. (4). The tactel output is almost linear in spite of the large deflections. This plot was generated from the average of seven trials to reduce small variations that may be caused by friction in the force device. The force application instrument is simply a balance beam with weights placed at one end and the 3.2-mm diameter probe halfway between the pivot point and the weight. There is a counterbalance weight on the opposite side of the pivot point. The tactel response to a 1-N load is 6% less than the straight line from the origin through the strain for a 0.5-N load. A strain of 10% is very large, even for a rubber material, and thus a nonlinear force-deflection relation is expected. This force-strain relation can easily be used in a look-up table to make an estimate of the "true" strain in the medium, but this wasn't needed here. This is the strain that would be sensed if the sensor and medium were truly linear. The deflection of a sample of rubber as a function of load was measured with a vernier and found to have a similar relation. The capacitor in the sensor appears to respond as the parallel plate capacitor of eq. (2).

### 3.1. Calibration

More important than raw sensitivity is the spatial performance of the sensor (that is, how the pressure measurement capabilities vary from element to elements and with the sensor geometry). A 3-mm diameter probe with a hemispherical tip is applied with a 50-gm load at 0.6-mm increments along the length of the cylinder, while the voltage outputs from seven elements of a row are recorded. The probe is applied for equal time to each location. The maximum percent deflection for each cell, the gain parameter, is stored

*Fig. 7. Responses along cylinder length for moving probe.*

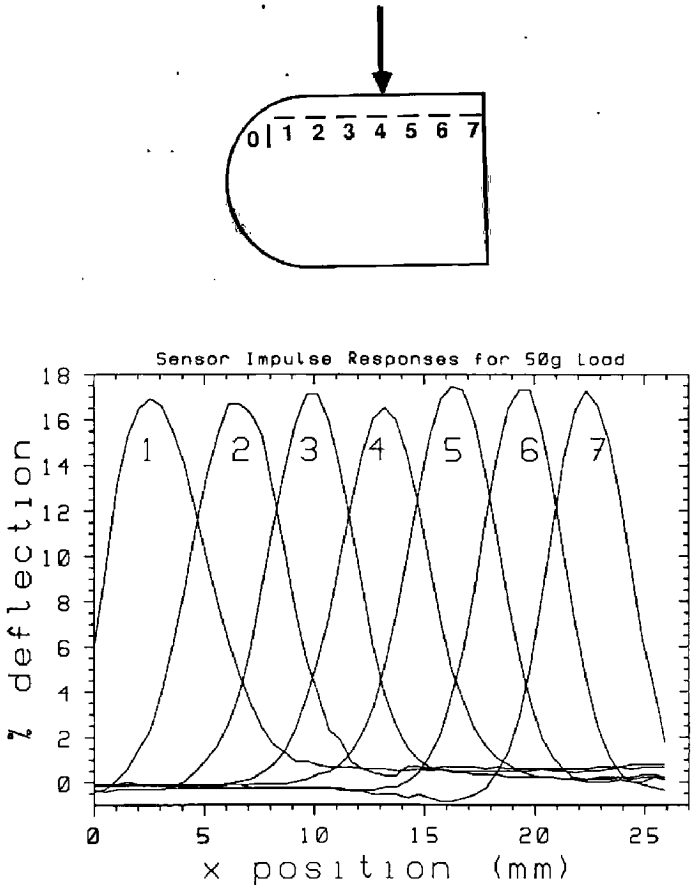


*Fig. 8. Sensitivity variation among tactels.*

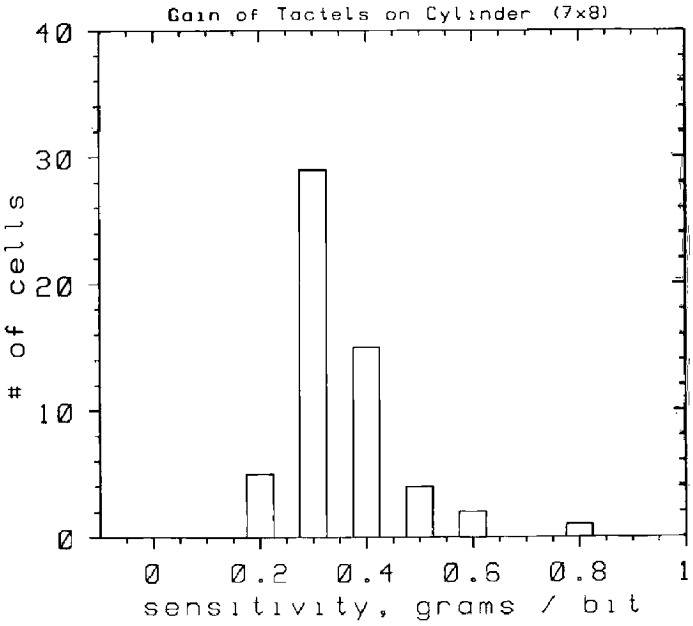


in a table and used to normalize the sensor output. There is some variation in gain, which can be caused by variations in the rubber dielectric as it is wrapped around the core during finger fabrication, giving different dielectric stiffness and thickness at different cells. Figure 7 shows the tactel responses along a row after calibration. There is good overlap between sensing elements, which is important for interpolation. Note the elastic set as the probe moves from the tip to the base (left to right in the figure), which can be seen at the right side of Figure 7 as residual deflection of elements at the tip when the probe is at the base. The tactel gains change for the first month after molding as the isoprene rubber cures further, but then stabilize to within about 5% of the calibrated gain value.

Figure 8 is a histogram of the sensitivities for all the $7 \times 8$ tactile elements on the cylindrical portion of the finger. The mean sensitivity threshold for a 1-unit change in the A/D converter is 0.4 grams with the $7.8\text{-mm}^2$ area probe. Five cells were very sensitive, with a threshold of only 0.2 grams. All the array elements are functional, and the worst element has a threshold of about 0.8 gram, which is still usable.The finger is designed for use with the Stanford/JPL hand, which in our configuration exerts up to 400 grams at each finger. We may have more than enough sensitivity with this tactile sensor for this hand.

### 3.2. Superposition

If the sensor behaves as a linear space invariant system, there are many powerful techniques from linear system theory that can be used to analyze it. If the sensor response is linear and obeys the principle of superposition, the linear space invariant assumption will hold. Figure 9 shows interpolated strain profiles for two probes applied independently and jointly. The sum of the individual strain profiles corresponds well to the joint strain profile. Thus superposition seems to be a valid assumption, at least with forces less than 100 grams or so.

Sensor hysteresis interferes with superposition in two ways. The first is that the sensor will not be time

*Fig. 9. Superposition of two loads on finger.*

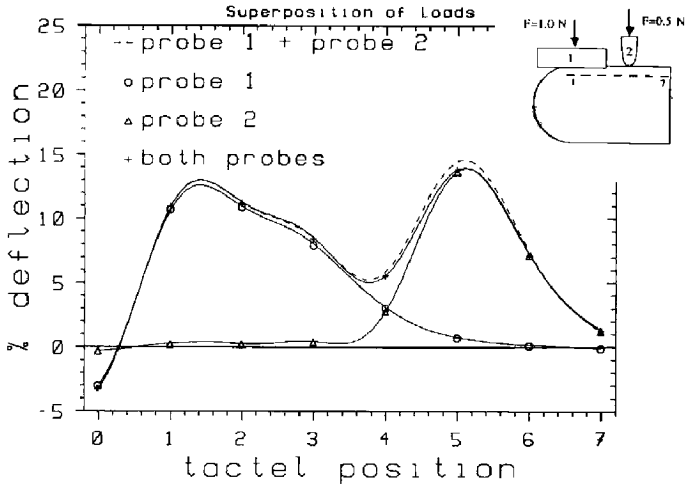


*Fig. 10. Sensor output jitter for repeated force.*

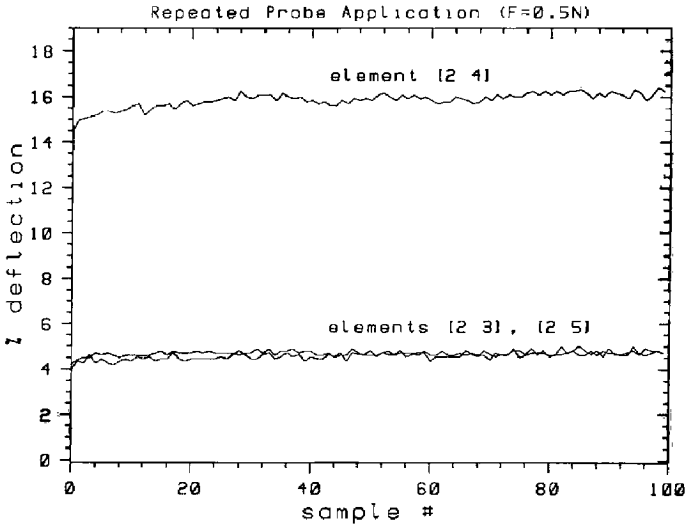


invariant. The second is that if the initial strain conditions are not zero, the sensor will not have a linear relation. Because of the offset, if the sensor output is described by $f(p)$ for some input load $p$, then $f(2p) = 2f(p) + \text{offset} \neq 2f(p)$.

### 3.3. Noise Limitations

With no load, the dominant sensor noise was found to be quantization from the A/D converter. The minimum detectable deflection of the capacitor in the sensor depends on the nominal capacitor output voltage $V_o$ (eq. 4). The smaller the voltage $V_o$ (implying larger plate separation), the larger the deflection quantization step size. A deflection of $\pm 0.05\%$ corresponds to about $\pm 0.3$ grams for the most sensitive cells shown in Figure 8. A force step quantization ($\Delta$) of 0.5 grams implies that the standard deviation of the sensitivity $S = \Delta/\sqrt{12} = 0.14$ grams.

The sensor output variation is higher when a 50-gram weight is repeatedly applied at the same location. Figure 10 shows the output jitter for a tactel directly beneath the probe and two adjacent tactels for 100 applications of the 50-gram weight. The histogram of the jitter is shown in Figure 11. The standard deviation of the signal under the probe is equivalent to a 1-gram weight variation. This error is caused by quantization and several balance beam errors. The force application errors are probably a result of a combination of location wobble of the probe, varying surface friction on the finger, friction in the balance pivot, and varying impact velocities as contact is made. Most experiments rely on only a single measurement, so these error sources can be neglected, since they will affect all tactel measurements simultaneously. Finger calibration accuracy is limited by these errors.

### 3.4. Viscoelastic Behavior

The price to pay for high sensitivity in a compliant sensor may be hysteresis. Soft polymers undergoing large deformations can be expected to exhibit elastic set and creep. The time response of the sensor to the 50-gm force steps of Figure 12 may be more useful than the traditional hysteresis loop to see the temporal effects of creep. The arrows in the figure indicate force applied, and dots indicate force removed. What is important is not just how much strain remains when the force is removed, but how long it takes to decay. The sensor shows the effects of creep strain, which is a continued flow of material, and a delayed elastic response (Johnson 1985). The creep strain causes problems, because it can make the sensor output appear as if too much force is being applied. The delayed elastic response makes it hard to determine whether contact

*Fig. 11. Probe noise histogram.*

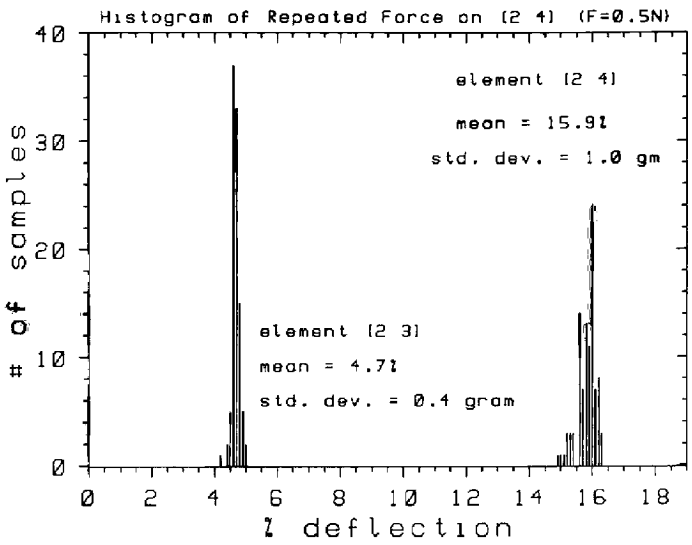


*Fig. 12. Viscoelastic response of sensor.*

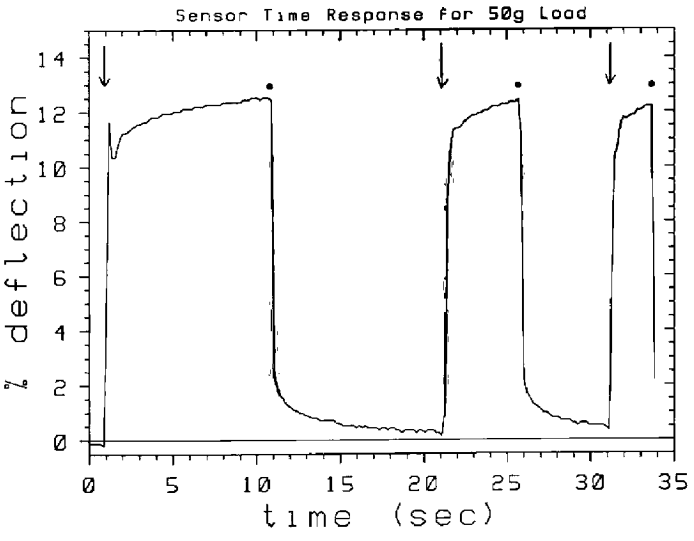


*Fig. 13. Response around circumference for moving probe.*

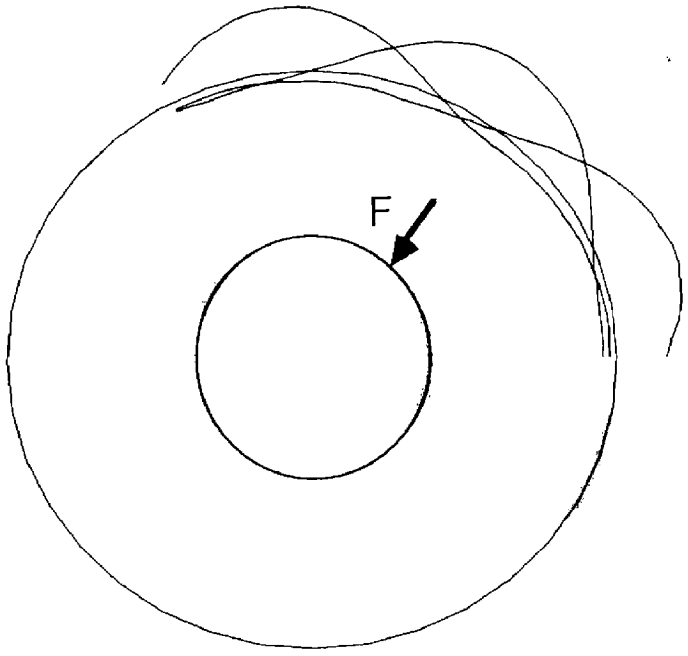


has been broken. If contact removal can be determined, one possible method for dealing with the residual strain is setting a new zero deflection point after contact is broken.

Delayed elasticity can set a practical upper limit to how fast the sensor should be scanned. For this sensor, it takes about 0.1 s for the response to decay to 10% of the peak fractional deflection, and the response is left with a residual deflection of about 5% of the peak fractional deflection. Beyond a 25-Hz scan rate or so, the delayed elastic response may represent a 25% sensor output error or greater. It will be hard to determine whether the deflection measurements are from a contact or a phantom remnant.

### 3.5. Response Around Circumference

Figure 13 shows three cells around the circumference for an earlier finger with 45° spacing as a probe is applied normally at 3° intervals around the circumference. There is sufficient response overlap, but it is not as good as along the finger length. The newest finger reduced this spacing to 18° to make the responses more uniform along the length and circumference. Fearing and Binford (1989) consider the response around the cylinder circumference in more detail.

### 3.6. Tip Behavior

The tip portion of the finger has been analyzed less extensively than the cylindrical portion. The core extends slightly into the tip area to improve sensitivity and to prevent a dead spot at the junction between the hemisphere and the cylinder. From the top of the

*Fig. 14. Responses for moving probe, normal to tip.*

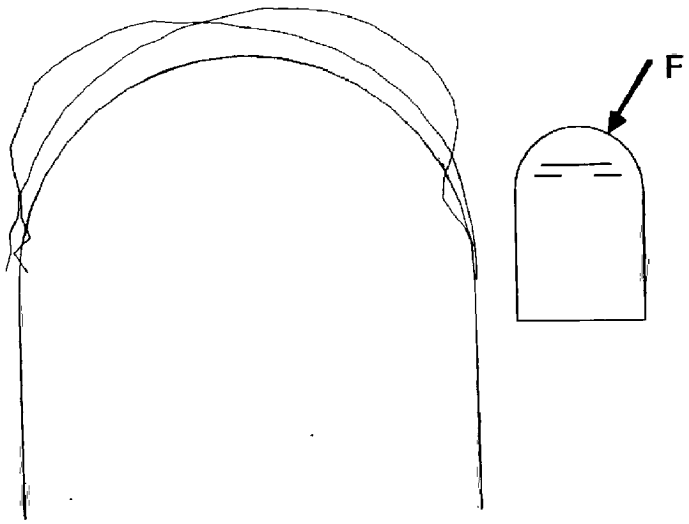


*Fig. 15. Finger geometry for plane stress assumption.*

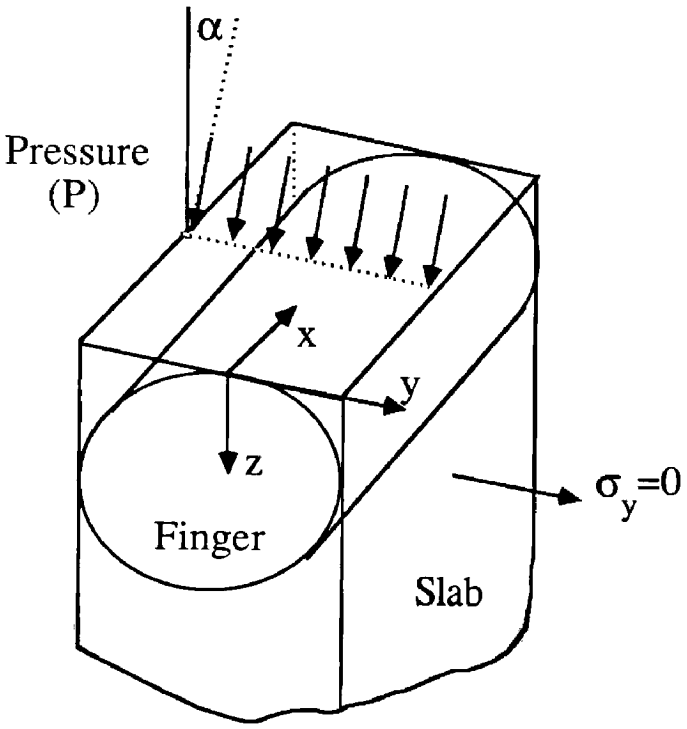


hemisphere to its base, the rubber is about 10 mm thick. The response for the tip with the force applied normal to the surface, as would be used for point contact grasping, is given for two elements in Figure 14. Not much analysis has been done on the tip yet because of the difficulty of analyzing the strain impulse responses of the sensing elements beneath the hemisphere. The space invariant assumption cannot be used for the tip, because the thickness of the medium is not constant above the sensors; it varies with position.

It would be reasonable to mount sensors on a hemisphere underneath the hemispherical tip. This was not done because of the added complexity of forming copper strips for capacitor plates on a nondevelopable surface.

## 4. Linear Elastic Model for Half Plane

A two-dimensional stress-strain analysis similar to that used in Phillips and Johnson (1981) and Fearing and Hollerbach (1985) will be used here to predict the strain and fractional capacitor deflection for stresses on the surface of a half plane. Figure 15 defines the finger coordinate axes. Capacitor deflection is defined in the $z$ direction for a sensor at the top of the cylinder. Consider a slice of elastic material in the $x$-$z$ plane, with the applied force on top constant in the $y$ direction and the stresses on the face of the slab ($\sigma_y$) equal to 0. This is the plane stress assumption. The slab corresponds to the cylindrical portion of the finger, and the thickness of the slab corresponds to the diameter of the cylinder in a crude way.

Fearing and Hollerbach (1985) used plane strain instead of plane stress, but they assumed infinite finger length. However, the responses of Figure 7 show closer agreement to the plane stress response, so that assumption will be used here.

The inclusion of three materials (rubber, dielectric, and copper) definitely makes the sensor nonisotropic. Of course, linear elasticity theory is only valid for small strains, which ours are not (up to 30%), but this is a reasonable first-order approximation. For a linear three-dimensional isotropic medium, the relations between the stresses and strains are (Timoshenko and Goodier 1951):

$$\epsilon_x = \frac{1}{E}[\sigma_x - \nu(\sigma_y + \sigma_z)]$$

$$\epsilon_y = \frac{1}{E}[\sigma_y - \nu(\sigma_x + \sigma_z)] \qquad (5)$$

$$\epsilon_z = \frac{1}{E}[\sigma_z - \nu(\sigma_x + \sigma_y)]$$

*Fig. 16. Plane stress model and experimental data.*

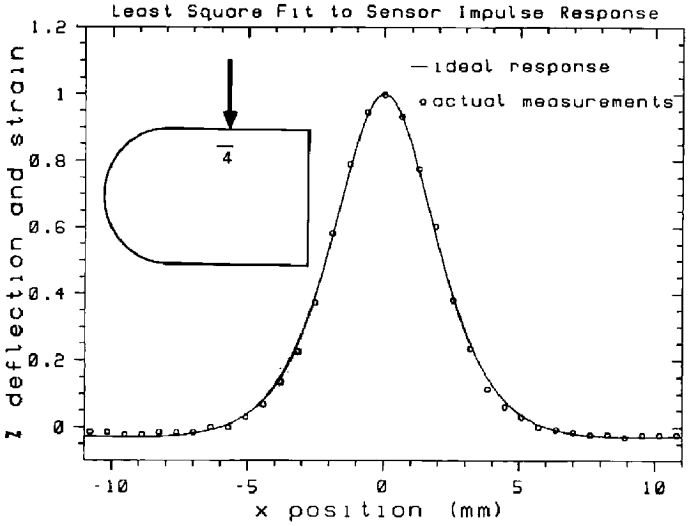


The strains in each direction are given by $\epsilon_x$, $\epsilon_y$, and $\epsilon_z$. The stresses are given by $\sigma_x$, $\sigma_y$, and $\sigma_z$. The parameter $\nu$ is Poisson's ratio, which is equal to 0.5 for an incompressible material like rubber. $E$ is Young's modulus, which is approximately $2.5 \times 10^5$ $Nm^{-2}$ for our finger. The stresses for a load normal to the surface are (Fearing and Hollerbach 1985):

$$\sigma_x = \frac{-2Pzx^2}{\pi r^4}, \qquad \sigma_z = \frac{-2Pz^3}{\pi r^4}, \tag{6}$$

where $P$ is the force per unit thickness of the slab in $Nm^{-1}$, and $r^2 = x^2 + z^2$. For the plane stress approximation, $\sigma_y = 0$. Thus for a line load and indentation at angle $\alpha$ from normal,

$$\begin{aligned} \epsilon_z &= \frac{1}{E}(\sigma_z - \nu\sigma_x) \\ &= \frac{-2P}{E\pi r^4}(z\cos\alpha - x\sin\alpha)(z^2 - \nu x^2). \end{aligned} \tag{7}$$

For the plane strain approximation, corresponding to $\epsilon_y = 0$ (an infinitely long line of force on an elastic half space),

$$\sigma_y = \nu(\sigma_x + \sigma_z). \tag{8}$$

$$\begin{aligned} \epsilon_z &= \frac{1+\nu}{E}[\sigma_z(1-\nu) - \nu\sigma_x] \\ &= \frac{-2Pz(1+\nu)}{\pi r^4 E}[z^2(1-\nu) - \nu x^2] \end{aligned} \tag{9}$$

A useful substitution from Gladwell (1980) shows the relation of plane stress to plane strain. By substituting the following into eq. (9),

$$\nu = \frac{\nu^*}{1-\nu^*} \tag{10}$$

where $\nu^*$ is the equivalent Poisson's ratio, the equivalence can be shown. For example, plane stress with $\nu = 0.5$ corresponds to plane strain with $\nu = 0.3333$.

### 4.1. Impulse Response Along Length

A knife edge (which approximates a line load) with 0.5 N was applied normally along the finger length at 0.6-mm increments while recording the output from one cell. A crude approximation to the finger is an elastic slab with a line load at the surface, which corresponds to the plane stress assumption of the previous section. Accordingly, after amplitude normalization, a least-squares fit to the plane stress model of eq. (7) was done by adjusting the depth and Poisson's ratio parameters. The best fitting parameters were a depth of 3.8 mm and $\nu = 0.4$. These parameters are consistent for most of the tactile elements in the array. The theoretical and experimental results are compared in Figure 16. The solid curve in the figure is predicted by the plane stress model with $d = 3.8$ mm and $\nu = 0.4$, with no free parameters. It is not an arbitrary best fitting curve to the experimental data.

Poisson's ratio ($\nu$) is equal to 0.5 for an incompressible material like rubber, but the dielectric layer has space for expansion, which gives the finger some overall compressibility. The rubber layer above the core is 3.8 mm thick, but this thickness is coincidental to the depth estimate. The top capacitor plate is at about 3.2 mm depth; it is postulated that the softer dielectric layer acts to spread the strain response out more, giv-

ing an effective greater depth without losing sensitivity. The root mean square (RMS) fitting error is just 1.3% of full scale, which is quite good considering that the standard deviation of a tactel output with a constant force of 0.5 N repeatedly applied above a cell by a balance beam is 2.0% of full scale. The assumption is made that this variance is caused by friction and positional jitter in the beam rather than by sensor variation. There is little variance in the experimental data that is not statistically explained by the model. The sensor performs with close to the ideal behavior of the plane stress model, in spite of violating the small deflection assumption of linear elasticity theory. Compensation for the nonlinearity of the sensor would help for larger loads; this experiment was done in the linear region of the sensor.

It is interesting to speculate why the sensor matches the model so well. The slab model may not be unreasonable; the contact length is small compared to the finger diameter. A rigid backing to the capacitors (the rigid core of the finger) does not affect the impulse response very much, as will be shown in the next section. The inhomogeneities caused by the copper strips in the sensor apparently do not have much effect. The copper may not be bonded very well to the rubber skin, which would allow the rubber to move independently of the copper. Thus the copper stiffness might not increase the overall rubber stiffness.

## 5. Linear Elastic Model for Strip

The plane stress model assumes that the capacitor is in an elastic medium of infinite extent and that the capacitor plates are very close to each other with respect to the sensor depth. Because of the core, a more accurate model would be an elastic strip with rigid foundation in two dimensions. This section models the effects of the finite thickness of the elastic medium on the impulse response. An important question for a given plate depth and separation is whether there should be a hard or soft foundation for the capacitor. Figure 3 shows the plane strip model. We will consider the dielectric layer and rubber to be rigidly attached to the core.

The deflections of the capacitor plates can be solved using elastostatic potential methods. Using the Papkovich-Neuber elastic potential (Gladwell 1980) with no body force, the displacement vector $\boldsymbol{d}$ is given as a function of a vector potential $\boldsymbol{\psi}$ and a scalar potential $\phi$:

$$2\mu \boldsymbol{d} = 2(1-\nu)\boldsymbol{\psi} - \nabla\{\boldsymbol{r}\cdot\boldsymbol{\psi} + \phi\} \tag{11}$$

where $\mu$ is the shear modulus, $\nabla^2\boldsymbol{\psi} = 0$ and $\nabla^2\phi = 0$, with

$$\boldsymbol{r} = x\hat{x} + y\hat{y} + z\hat{z} \quad \text{and} \quad \boldsymbol{\psi} = \psi_1\hat{x} + \psi_2\hat{y} + \psi_3\hat{z}. \tag{12}$$

The displacement vector has three displacement components: $\boldsymbol{d} = u\hat{x} + v\hat{y} + w\hat{z}$. The shear modulus $\mu$ is related to Young's modulus $E$ and Poisson's ratio $\nu$ by:

$$\mu = \frac{E}{2(1+\nu)}. \tag{13}$$

The deflections for the two dimensional case from Gladwell (1980):

$$2\mu u = 4(1-\nu)\psi_1 - \frac{\partial}{\partial x}(x\psi_1 + z\psi_3 + \phi) \tag{14}$$

$$2\mu w = 4(1-\nu)\psi_3 - \frac{\partial}{\partial z}(x\psi_1 + z\psi_3 + \phi) \tag{15}$$

where $\psi_1$, $\psi_3$, and $\phi$ are plane harmonic functions,

$$\left(\frac{\partial^2}{\partial x^2} + \frac{\partial^2}{\partial z^2}\right)(\psi_1, \psi_3, \phi) = 0. \tag{16}$$

The strains are obtained from the displacements by:

$$\epsilon_x = \frac{\partial u}{\partial x}, \quad \epsilon_z = \frac{\partial w}{\partial z}, \quad \gamma_{zx} = \frac{1}{2}\left(\frac{\partial u}{\partial z} + \frac{\partial w}{\partial x}\right), \tag{17}$$

where $\gamma_{zx}$ is the shear strain. The stresses for plane strain are obtained from the strains via:

$$(1-2\nu)\sigma_x = 2\mu[(1-\nu)\epsilon_x + \nu\epsilon_z] \tag{18}$$

$$(1-2\nu)\sigma_z = 2\mu[(1-\nu)\epsilon_z + \nu\epsilon_x] \tag{19}$$

$$\tau_{xz} = 2\mu\gamma_{xz}, \tag{20}$$

where $\tau_{xz}$ is the shear stress. For the plane stress approximation, the substitution $v^* = v/(1 + v)$ gives the corresponding stresses (Gladwell, 1980).

For an elastic strip of thickness $h$, appropriate potential functions to choose are $\psi_2 = 0 = \psi_3$; given in Fourier transform representation (Gladwell 1980), the other potentials are:

$$\psi_1(x, z) = F^{-1}\{s^{-1}[A(s)e^{-sz} + B(s)e^{sz}]\} \quad (21)$$

$$\phi(x, z) = F^{-1}\{s^{-2}[C(s)e^{-sz} + D(s)e^{sz}]\} \quad (22)$$

where $s$ is spatial frequency, and $F^{-1}\{\ \}$ is the inverse Fourier transform.

The boundary conditions for the strip, assuming frictionless indentation at the surface, are,

$$\tau_{xz}(x, z = 0) = 0 \quad (23)$$

and for perfect adhesion at the bottom of the layer,

$$u(x, z = h) = 0 \quad (24)$$

$$w(x, z = h) = 0. \quad (25)$$

Gladwell (1980) gives the solution for frictionless contact at the foundation; here the adhesive contact is found. The normal stress at the surface must equal the applied pressure, so

$$\sigma_z(x, z = 0) = p(x), \quad (26)$$

where $p(x)$ is the contact pressure.

With four equations for the four unknowns $A$, $B$, $C$, and $D$, the system of equations can be solved. The deflection normal to the surface is given by

$$2\mu w(x, z) = F^{-1}\{P(s)H(s, z)\}. \quad (27)$$

Finally, after matching boundary conditions, the kernel $H(s, z)$ is obtained:

$$H(s, z) = \frac{1}{s}[(\kappa A + szA + C)e^{-sz} + (\kappa B - szB - D)e^{sz}]. \quad (28)$$

The terms in the above are expanded as:

$$\alpha = \frac{-\kappa e^{2\omega} + 2\omega - 1}{\kappa e^{-2\omega} + 2\omega + 1} \quad (29)$$

$$B(s) = \frac{e^{-\omega} + e^{\omega}}{e^{-\omega}[\alpha(\kappa - 2\omega) - 1] + e^{\omega}(\alpha - \kappa - 2\omega)} \quad (30)$$

$$A(s) = \alpha B(s) \quad (31)$$

$$-D(s) = \frac{A[\omega - (1 - 2v)]e^{-\omega} + B[\omega e^{\omega} - (1 - 2v)]e^{-\omega}}{e^{-\omega} + e^{\omega}} \quad (32)$$

$$C(s) = D - (1 - 2v)(A + B) \quad (33)$$

where $\omega = sh$, with $h$ the thickness of the layer, and $\kappa = 3 - 4v$. Because $H(s)$, $P(s)$ are even and real functions, the inverse cosine transform can be used to determine deflection:

$$2\mu w(x, z) = 2\int_0^{\infty} P(s)H(s, z) \cos 2\pi sx ds \quad (34)$$

To determine sensor gain (the percent deflection) at a certain depth $d$, it is necessary to know the deflection directly beneath the center of pressure, $w(x = 0, z = d)$. The previous equation simplifies to:

$$2\mu w(0, z) = 2\int_0^{\infty} P(s)H(s, z)ds. \quad (35)$$

The gain for the capacitor at a certain depth is given by

$$\text{gain} = \frac{\Delta z}{d_o} = \frac{w(0, z = d)}{h - d}, \quad (36)$$

with $d_o$ the nominal capacitor plate separation as previously. The gain for plane stress is shown in Figure 17 for two cases, where the surface pressure in the plane is taken as a parabola of the probe width, 3 mm. In the first case the medium is 3.8 mm thick, and the gain is plotted as a function of the depth of the top plate of the capacitor. The bottom plate is fixed at the foundation, so this case also shows gain as a function of nominal plate separation, $d_o$. The gain does not go to zero even when the top plate gets close to the boundary layer. Although the gain is slightly reduced, the actual capacitance value gets larger, so there is more signal to work with.

In the second case, the capacitor bottom plate is at 3.8 mm depth, and the plate separation $d_o$ is fixed at

*Fig. 17. Gain vs. capacitor separation and strip thickness.*

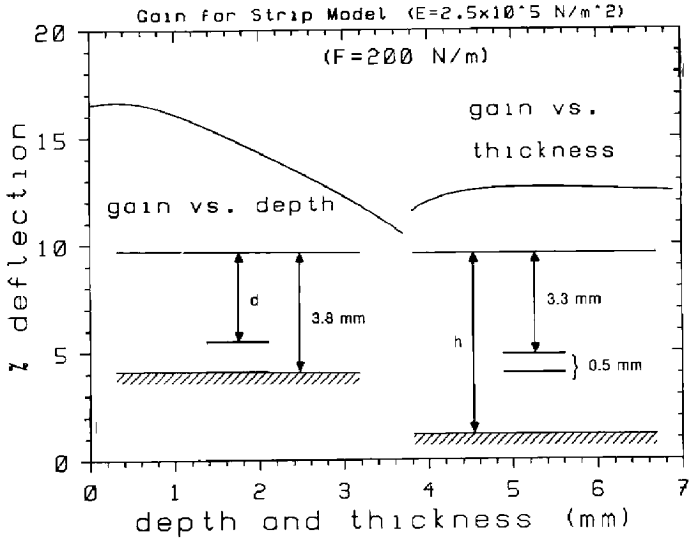


*Fig. 18. Impulse response for half plane and strip.*

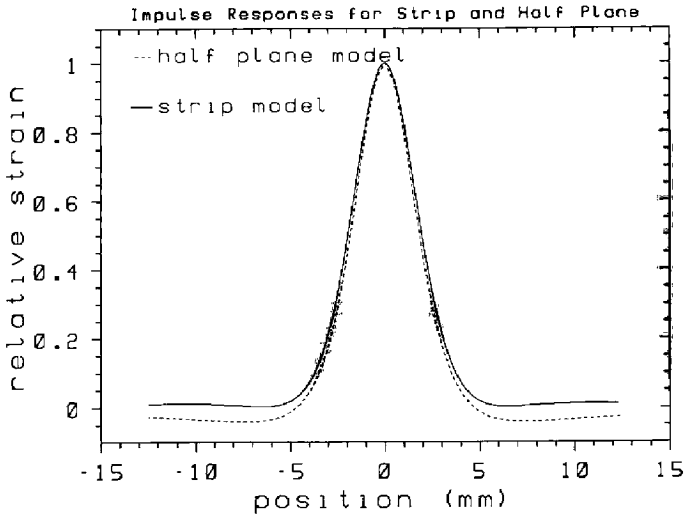


0.5 mm. The gain is plotted as the thickness of the layer beneath the capacitor increases, so the capacitor now has a soft backing. As can be seen from the plot, the increased thickness does not substantially increase the sensor gain. It is apparently not necessary to have a capacitor above a compliant foundation to obtain adequate sensitivity.

This model predicts about 10% deflection for the same parameters as used in the finger calibration (Fig. 7) ($d_o = 0.5$ mm, $h = 3.8$ mm, and $F \approx 200$ Nm$^{-1}$), which agrees well with the experimental value. As the layer beneath the capacitor gets thicker, the model should approach the infinite half plane of the previous section. Because gain changes so little with increasing thickness, it seems reasonable to use the much simpler plane stress half plane analysis of the previous section. As shown in Figure 18, the impulse response for the plane strip is quite similar to the impulse response for the half plane in shape and width. The half plane model agrees more closely with experimental data. The dielectric layer is softer than the skin above it and may cause this effect. The multiple elastic layer problem has not been considered here.

From the plane strip analysis, it can be concluded that a soft backing for the bottom capacitor plate is not required; it can be attached to a rigid foundation with no significant loss of sensitivity. The rigid foundation makes fabrication much simpler. The plane strip model does not yield a closed form expression for the impulse response, but the calculated impulse response is similar enough to the plane stress half plane assumption that the half plane assumption should be adequate for experimental analysis along the length of the finger.

## 6. Strain Signal Reconstruction

From discrete strain measurements, it is useful to recover a continuous signal. Because of the coarse spacing of sensors along the length of the cylindrical portion of the finger, localization to much better than the tactel spacing is important to get good position information. The recovery of peak deflection is also important for estimating load magnitudes on the finger. This section describes an interpolation method for recovering location and magnitude of the center of pressure from discrete measurements. A better analysis for a restricted contact type is in Fearing and Binford (1989).

Assume discrete sensors at spacing $b$; then seven sensors of one row along the cylinder give

$$\epsilon_z[x] = h(x) \sum_{n=-\infty}^{\infty} \left[ \delta(x - nb) \operatorname{rect}\left(\frac{x}{3b}\right) \right], \quad (37)$$

*Fig. 19. Frequency response $H(s)$ and aliased response $A(s)$.*

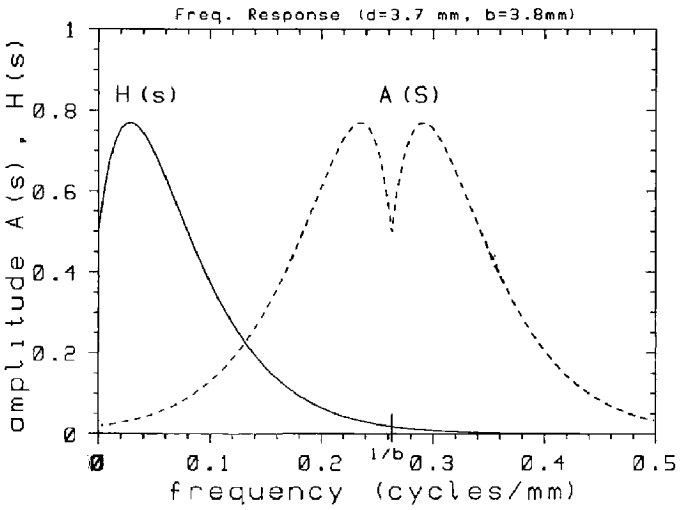


where $h(x)$ is the normal strain impulse response from eq. (8), defined by

$$h(x) = \frac{-2z}{\pi E r^4}[z^2 - \nu x^2]. \tag{38}$$

The rect ( ) function is defined by

$$\text{rect}(x) = \begin{cases} 1 & \text{if } |x| \leq 1 \\ 0 & \text{if } |x| > 1 \end{cases} \tag{39}$$

In the frequency domain, eq. (38) leads to

$$E_z(s) = H(s)^* \frac{1}{b} \sum_{n=-\infty}^{\infty} \left[ \delta\left(s - \frac{n}{b}\right)^* 6b \,\text{sinc}\,(6\pi bs) \right], \tag{40}$$

with spatial frequency $s$ in cycles/mm and $E_z(s)$ the Fourier transform of $\epsilon_z(x)$. Because of sampling, $E_z(s)$ is periodic in frequency, and the frequency response is widened by the convolution with the sinc $(6\pi bs)$ term, which is a result of having only seven samples. The frequency response of $h(x)$ (eq. 39) at depth $z = d$ with the plane stress assumption is given by

$$\begin{aligned} H(s) &= 2\pi d\left(|s|(1+\nu) + \frac{1-\nu}{2\pi d}\right)\frac{e^{-2\pi d|s|}}{E} \\ &= \left(3\pi d|s| + \frac{1}{2}\right)\frac{e^{-2\pi d|s|}}{E}. \end{aligned} \tag{41}$$

The maximum response occurs at $s = 1/3\pi d$. Figure 19 shows the frequency response for $d = 3.8$ mm. If we assume that integration of deflection occurs along the capacitor plate, the finite sensor width may improve the low-pass properties of $H(s)$ slightly. The aliasing energy is significant but is reduced in practice by low-pass contact pressure distributions.

The continuous signal can in principle be recovered by low-pass filtering of the periodic spectrum $E_z(s)$, but this process is limited by aliasing and the finite extent of $\epsilon_z[x]$. Ignoring the finite finger length for now, with ideal low-pass filtering we have

$$\tilde{E}_z(s) = E_z(s)\,\text{rect}\,(2bs). \tag{42}$$

The low-pass filtered version has both the desired and the aliased components

$$\tilde{E}_x(s) = [H(s) + A(s)]\,\text{rect}\,(2bs), \tag{43}$$

where $A(s)$ is the aliased spectrum neglecting higher order terms, given by

$$A(s) = H\left(\frac{1}{b} + s\right) + H\left(s - \frac{1}{b}\right). \tag{44}$$

The relative error caused by aliasing is obtained from the ratio of energy in the reconstruction error $(E_o - E_R)$ to the energy in the original signal $(E_o)$ (Pratt 1978). Assuming an ideal low-pass filter, the error is given by:

$$\xi = \frac{E_o - E_R}{E_o} = \frac{\int_{-\infty}^{\infty} |H(s)|^2 ds - \int_{-1/2b}^{1/2b} |H(s)|^2 ds}{\int_{-\infty}^{\infty} |H(s)|^2 ds}. \tag{45}$$

This expression includes reconstruction errors caused by the cutoff of the high frequencies of $H(s)$. Not included are the effects of nonideal low-pass filtering. Evaluated numerically for the sensor depth and 3.8-mm spacing, we get $\xi \approx 0.20$, which implies up to 20% error for localization and amplitude in the interpolated function $\epsilon_x(y)$. If $P(s)$ is sufficiently bandlimited, eq. (45) will be an upper bound on the expected error.

The effects of aliasing on localization and amplitude

*Fig. 20. Reconstruction error caused by aliasing ($b = 3.8$ mm).*

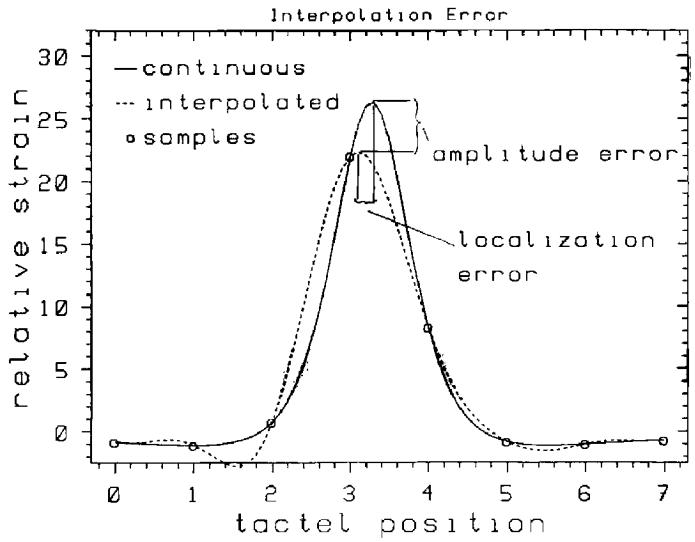


*Fig. 21. Interpolated deflection surface.*

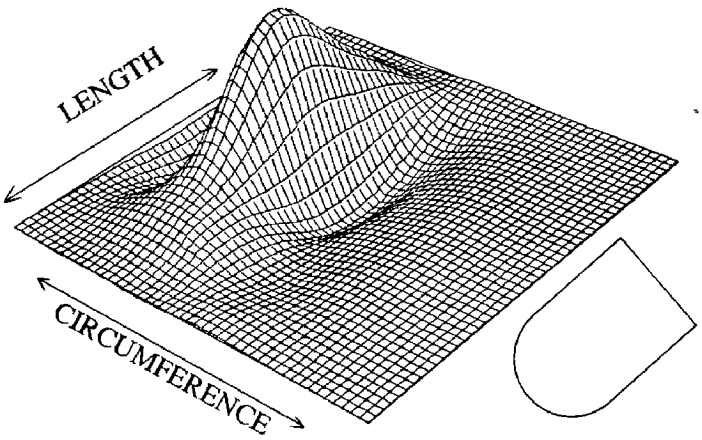


estimation will now be shown for the seven sensors along a row on the finger. The strain response estimate using a windowed sinc interpolation is

$$\hat{h}(x_o) = d \sum_{n=2-3}^{3} \frac{\sin \pi(x_o - nb)}{\pi(x_o - nb)} w\left(\frac{x_o}{b} - n\right) h[nb] \quad (46)$$

with the Hanning window (Oppenheim and Schafer 1975), which is

$$w(n) = \frac{1}{2}\left[1 - \cos\left(\frac{2\pi n}{N-1} + \pi\right)\right], \quad \text{for } |n| \leq \frac{N-1}{2}, \quad (47)$$

and $N$ is the total number of samples. The window makes the low-pass filter finite in extent and reduces ringing. Figure 20 shows the peak displacement and amplitude error for the interpolated response to a point force in the plane stress model when compared to the continuous strain response.

## 7. Localization

It is important to know the contact location to apply forces accurately [see for example, Fearing (1986)]. Small location errors can lead to large force errors in certain finger configurations. Localization of a line force could in principle be done by solving for location, angle of force, and magnitude of force from the strain equations at three sensors as was proposed in Fearing and Hollerbach (1985). A more general approach when there is no tangential force at the surface and the applied pressure is an even, single maximum function, is to find the peak strain by interpolation. This simple scheme is relatively accurate but can be time consuming and is used mainly for sensor evaluation rather than as a real-time processing tool.

Let $z[i, j]$ be an $8 \times 8$ array formed from the simultaneous response of all the tactels, where $z[i, j]$ is the percent deflection of element $ij$. The interpolated deflection function is

$$f(x, y) = \sum_{i=0}^{N-1} \sum_{j=0}^{N-1} z[i, j] \frac{\sin \pi(x - i) \sin \pi(y - j)}{\pi^2 (x - i)(y - j)} w(x - i) w(y - j). \quad (48)$$

Here $x$, $y$ are in tactel spacing units where distances are normalized by dividing by the sensor spacing $b$. Figure 21 shows a plot of the deflection surface for contact with a large soft object (another finger), where the cylinder and the tip are "unwrapped" onto a plane.

A more useful tool than the surface plot for analyzing the sensor output is a plot of equal percent deflection contours. The conditions for equal deflection contours of height $k$ are:

$$f(x, y) = k, \quad \frac{\partial f}{\partial x} = f_x = 0, \quad \frac{\partial f}{\partial y} = f_y = 0. \quad (49)$$

*Fig. 22. Deflection contours on 8 × 8 array.*

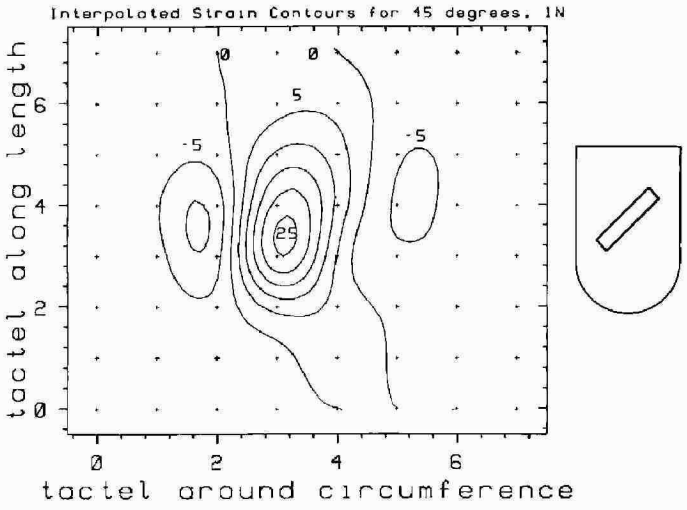


*Fig. 23. Measured probe location.*

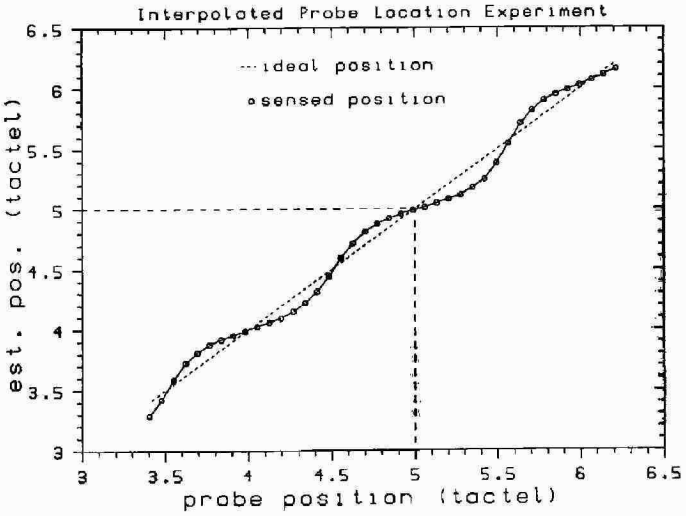


The direction of constant height on the surface is given by

$$\phi = -\tan^{-1}\frac{f_x}{f_y}. \tag{50}$$

The contours are found iteratively from

$$\Delta x = \begin{pmatrix} \Delta r \cos\phi \\ \Delta r \sin\phi \end{pmatrix}, \tag{51}$$

where $\Delta r$ is the step size. The height error at the new location, $f(x + \Delta x) - k$, is used to adjust the new $x$ and $y$ locations to ensure staying on the contour. Figure 22 shows the output of this contour tracking algorithm for a contact with a rod at 45° to the finger cylinder axis, where the finger has 45° by 3.8-mm sensor spacing. The low-pass characteristic ensures that the deflection surface is well behaved. The 45° spacing around the circumference is not sufficient, as the strain profile decreases to zero at just one tactel unit spacing around the circumference. Note how the cylinder bulges out at about ±90° from the contact location on the cylinder. This may be caused by the copper rings as well as by the incompressibility of the rubber.

To find the maximum deflection and its location for an unknown pressure, iterative techniques are needed. The conditions for a maximum of a surface are:

$$\frac{\partial f}{\partial x} = 0, \quad \frac{\partial f}{\partial y} = 0, \quad \frac{\partial^2 f}{\partial x^2} < 0, \quad \text{and} \quad \frac{\partial^2 f}{\partial y^2} < 0. \tag{52}$$

Using Newton-Raphson search (Thomas 1968) to find where the slopes are zero, we have

$$\begin{pmatrix} \Delta x \\ \Delta y \end{pmatrix} = -\begin{pmatrix} \frac{\partial^2 f}{\partial x^2} & \frac{\partial^2 f}{\partial x \partial y} \\ \frac{\partial^2 f}{\partial y \partial x} & \frac{\partial^2 f}{\partial y^2} \end{pmatrix}^{-1} \begin{pmatrix} \frac{\partial f}{\partial x} \\ \frac{\partial f}{\partial y} \end{pmatrix}. \tag{53}$$

Convergence to 0.01 tactel starting from the max $z[i, j]$ tactel is observed in typically two or three steps. Figures 23 and 24 show recovery of probe location and peak percent deflection along the central portion of the cylinder to avoid boundary effects. A 50-gm load is centered above a strip. The error will be higher if the probe is between the copper strips. The probe is moved at 250-$\mu$m increments along the strip (the tactile elements are spaced 3.8 mm along the row). The abscissas in the figures are given in tactile element (tactel) spacing units.

The ripple on amplitude and peak location is mainly caused by aliasing. The position of the probe and amplitude are sensed within ±12% of ideal for a positioning error of ±0.5 mm along the length of the finger. These results imply that aliasing is less severe than

*Fig. 24. Measured peak amplitude.*

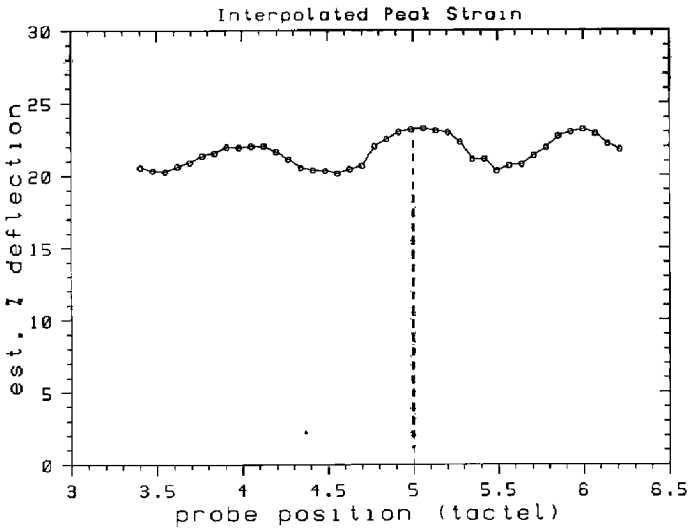


*Fig. 25. Localization errors around circumference.*

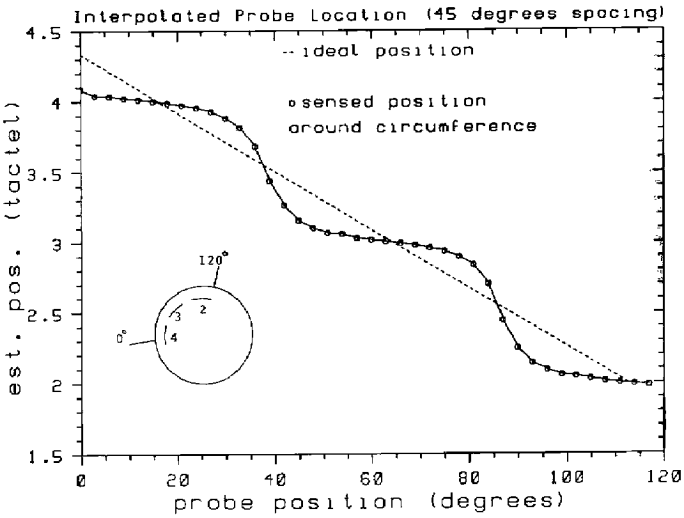


predicted by the simple plane stress model with a line load. Note that the aliasing error is zero when the probe is directly above a tactel, because the sinc interpolation passes through the sample points. An additional source of errors is the nonuniform positioning of the sensor rings from manufacture.

Localization performance around the circumference of the finger was tested in the same manner by applying the probe at 3° increments. The localization error is larger, about ±10° (Fig. 25). This is about ±2.3-mm error along the circumference. To determine the orientation of a line contact on the finger cylinder, we need good localization along the length and around the circumference (Fearing 1987a). The error around the circumference was too large, so improved fingers were built with 18° spacing.

## 8. Estimating Total Force

It is useful to know the total normal force on the finger sensor. This section uses a simple approximation to estimate this force. For contacts longer than two or three times the sensor depth, $H(s)$ can be crudely approximated as constant, because the surface pressure $P(s)$ will tend to be bandlimited:

$$H(s) \approx H(0) = \frac{1}{2E}. \tag{54}$$

Then for a normal force,

$$\begin{aligned} \int_{x=-\infty}^{\infty} \epsilon_z(x)dx &= \int_{x=-\infty}^{\infty} F^{-1}\{H(s)P(s)\}dx \\ &\approx \int_{x=-\infty}^{\infty} H(0)F^{-1}\{P(s)\}dx \end{aligned} \tag{55}$$

and

$$\int_{x=-\infty}^{\infty} H(0)F^{-1}\{P(s)\}dx = \frac{\int_{x=-\infty}^{\infty} p(x)dx}{2E} \sim F_z, \tag{56}$$

where $F_z$ is the total force in the normal direction, and $\epsilon_z(x)$ is recovered by interpolation. Figure 26 shows the interpolated fractional deflection profile for three different contact lengths, each with a 50-gram load. The integrals of fractional deflection do not show large disagreement in spite of the crude approximation. Aliasing can contribute to errors in the integrals. Fearing (1987b) has a description of a more accurate method using an inverse filter, but the method here is simple and fast for large contact areas.

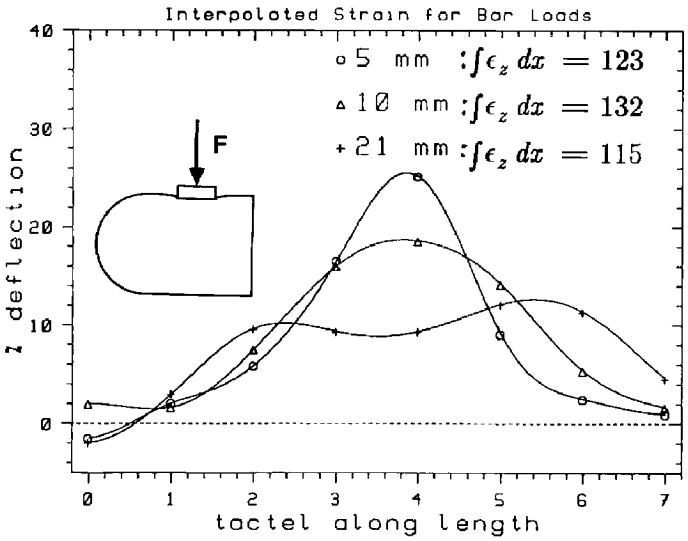


*Fig. 26. Contacts and total contact load.*

## 9. Recovering Force Angle

It would be useful to get tangential force information as well as normal pressure information from a tactile sensor. From eq. (8), the expression for normal strain with the plane stress assumption for a line load, it can be seen that normal and tangential surface stresses both contribute to the normal strain. Methods have been proposed for recovering the angle of force for line and cylindrical contacts (Fearing and Hollerbach 1985), where the contact type is known a priori. A method is proposed here for the case when the contact pressure is an even function (for example, symmetric contacts with edges, vertices, planes, spheres, and cylinders).

The normal stress corresponds to an even strain function, and the tangential stress corresponds to an odd function, as can be seen by breaking eq. (8) into even and odd components:

$$\begin{aligned}\epsilon_z &= \epsilon_{z\text{even}} + \epsilon_{z\text{odd}} \\ &= \frac{-2P}{E\pi r^4}[z(z^2 - \nu x^2)\cos\alpha] - \frac{-2P}{E\pi r^4}[x(z^2 - \nu x^2)\sin\alpha].\end{aligned} \tag{57}$$

Similarly, there are even and odd impulse responses $h_{\text{even}}(x)$, $h_{\text{odd}}(x)$.

The assumption can be made that the tangential stress at the surface at any point is proportional to the normal stress there (Smith and Liu 1953), that is:

$$\sigma_z(x, z=0) = p(x) \quad \text{and} \quad \sigma_x(x, z=0) = \beta p(x), \tag{58}$$

where $\beta = \tan\alpha$. Now for the normal strain at the sensor at constant depth $d$ caused by an even pressure distribution $p(x) = p(-x)$, we have by convolution:

$$\begin{aligned}f(x) &= f_{\text{even}}(x) + f_{\text{odd}}(x) \\ &= \int_{x_o=-\infty}^{\infty} p(x - x_o)[h_{\text{even}}(x_o, d) + h_{\text{odd}}(x_o, d)]dx_o,\end{aligned} \tag{59}$$

where $f(x)$ is the strain at $(x, z = d)$ caused by the pressure on the surface. The convolution of two even functions results in an even function, and the convolution of an even and an odd function results in an odd function. Thus the normal and tangential stress components result respectively in

$$f_{\text{even}}(x) = \int_{x_o=-\infty}^{\infty} p(x - x_o)h_{\text{even}}(x_o, d)dx_o \tag{60}$$

and

$$f_{\text{odd}}(x) = \int_{x_o=-\infty}^{\infty} p(x - x_o)h_{\text{odd}}(x_o, d)dx_o. \tag{61}$$

The measured and interpolated deflection function gives us even and odd parts by:

$$\begin{aligned}f_{\text{even}}(x) &= \frac{f(x) + f(-x)}{2} \\ f_{\text{odd}}(x) &= \frac{f(x) - f(-x)}{2}.\end{aligned} \tag{62}$$

A skew index is defined as

$$\text{skew} = \frac{\max f_{\text{odd}}}{\max f_{\text{even}}}, \tag{63}$$

which gives an indication of the relative force angle. Note that the skew index will be zero for pure normal indentation. In general, the skew index will be a complicated function of the pressure distribution and might best be used as a means of tracking force angle changes.

The skew index can be simply evaluated for a line

*Fig. 27. Even and odd strain components from model.*

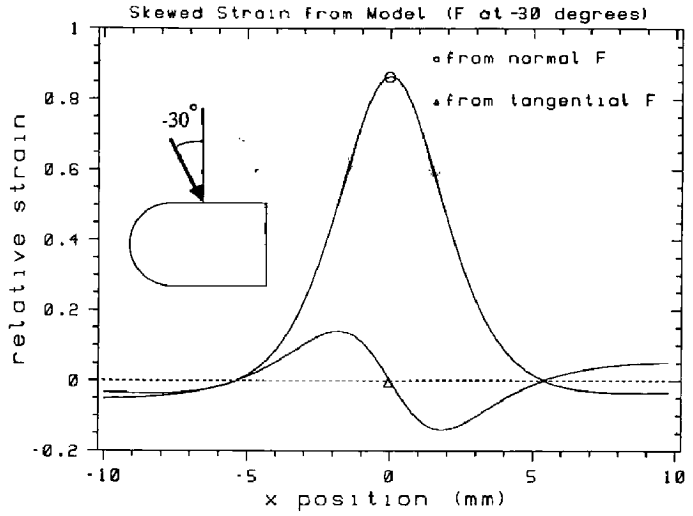


*Fig. 28. Measured even and odd percent deflection for ±30° contact.*

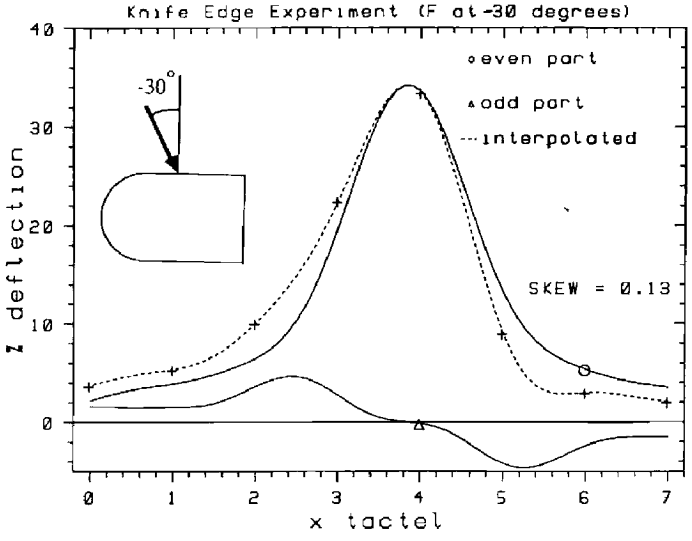


A

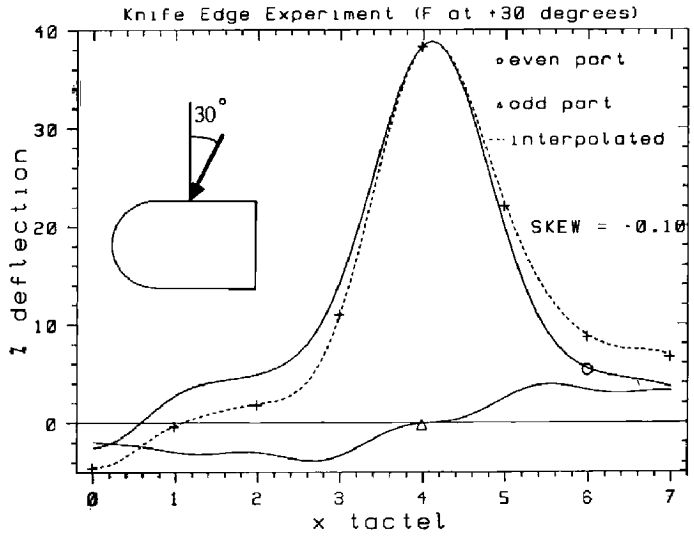


B

indentor. Unfortunately, for the plane stress assumption with $\nu = 0.5$, this is a low-fidelity signal for small force angles. The maximum even strain occurs at $y = 0$ and is given by

$$\max \epsilon_{z\text{even}} = \frac{-2P \cos \alpha}{\pi E_z}. \tag{64}$$

The maximum odd strain occurs at

$$x = z\left[\frac{3(1+\nu) - \sqrt{9(1+\nu)^2 - 4}}{2\nu}\right]^{1/2} \tag{65}$$

and the maximum odd strain for $\nu = 0.5$ is given by

$$\max \epsilon_{z\text{odd}} \approx \frac{-2P(0.2441) \sin \alpha}{\pi E_z}. \tag{66}$$

The ratio of odd to even strain is:

$$\frac{\max \epsilon_{z\text{odd}}}{\max \epsilon_{z\text{even}}} \approx 0.2441 \tan \alpha. \tag{67}$$

Figure 27 shows the analytic result for a line force at $\alpha = -30°$, and Figure 28 gives experimental results for a knife edge driven into the surface at $\alpha = \pm 30°$ from normal with 100-gm force. The strain response is recovered by interpolation from the seven tactels along the edge of the cylinder. Since the maximum even strain corresponds to the maximum strain response, the even and odd functions are determined with this point as the origin. The experimental result of about 0.1 for the skew ratio agrees well with eq. (67); however, a 10% signal can be obscured by hysteresis and calibration errors. Amplitude errors caused by aliasing are also a problem. Strain gauge methods may offer improved force angle recovery (Brock and Chiu 1985).

For a more general even pressure distribution than the line load, the force angle can also be obtained by

using inverse filtering. Taking Fourier transforms of the even and odd impulse responses, we have

$$h_{\text{even}}(x) \rightarrow H_n(s), \tag{68}$$

which is a real function (the frequency response for the normal component of surface stress), and

$$h_{\text{odd}}(x) \rightarrow H_t(s), \tag{69}$$

which is an imaginary function (the frequency response for the tangential component of surface stress). The strain is given by:

$$E_z(s) = P(s)[H_n(s) + \beta H_t(s)]. \tag{70}$$

Since $P(s)$ is real, the total pressure and angle can be solved (assuming the existence of the inverse filter) by

$$P(s) = H_n^{-1}(s)\ \text{Re}\ \{E_z(s)\} \tag{71}$$

and

$$\beta P(s) = H_t^{-1}(s)\ \text{Im}\ \{E_z(s)\}. \tag{72}$$

The limitations of inverse filtering are discussed in Fearing and Binford (1989). This method has not been tried experimentally.

## 10. Conclusion

Simple elastic models were used both to design the tactile sensor and to develop low-level interpretation strategies for the tactile data. A feature of this sensor is that it is encapsulated in a cylindrical finger with a hemispherical tip. The sensitivity of the sensor is adequate for many manipulation tasks. Using interpolation techniques, localization of applied forces is to within 0.2 tactel, and pressure estimation is to within 20%. These initial results are already sufficient to improve manipulation reliability greatly for the Stanford/JPL hand if a tactile servo system were available.

Perhaps the biggest improvements required are the need to reduce aliasing and the delayed elastic response. Some of the creep may be caused by imperfect adhesion between the rubber and copper strips, which allows partial slip at their interface. A more homogeneous sensor using compliant conductors would be easier to analyze. It is very hard now to account for the effects of the stiff inclusions of copper in the rubber; it is not an isotropic medium. Presently these effects are ignored but do not seem to cause large discrepancies from the theoretical response.

## Acknowledgments

Many thanks to A. Rise and G. Gorali, whose collaboration in sensor design and fabrication was invaluable; to T. Binford for guidance, insight, and encouragement; and to B. Armstrong and S. Shekhar for helpful comments. This work was performed while the author was a graduate student at Stanford University, with funding provided by DARPA contracts MDA903-86-K-0002 and F33615-82K-5108.

## References

Allen, P., and Bajczy, R. 1985 (Los Angeles). Object recognition using vision and touch. *9th Int. Joint Conf. on Artificial Intelligence,* pp. 1131–1137.

Begej, S. 1988. Planar and finger-shaped optical tactile sensors for robotic applications. *IEEE J. Robot. Automat.* 4(5):472–484.

Bicchi, A., and Dario, P. 1987 (August, Santa Cruz, California). Intrinsic tactile sensing for artificial hands. In Bolles, R., and Roth, B. (eds.): *Proc. of the 4th Int. Symp. on Robotics Research.* Cambridge, Mass.: MIT Press.

Boie, R. A. 1984 (Atlanta). Capacitive impedance readout tactile image sensor. *IEEE Int. Conf. on Robotics and Automation,* pp. 370–378.

Boie, R. A., and Miller, G. L. 1985. Conformable tactile sensor. U.S. Patent #4,526,043.

Brock, D., and Chiu, S. 1985 (Miami). Environment perception of an articulated robot hand using contact sensors. *ASME Winter Annual Meeting,* pp. 89–96.

Cameron, A., Daniel, R., and Durrant-Whyte, H. 1988

(Philadelphia). Touch and motion. *IEEE Int. Conf. on Robotics and Automation,* pp. 1062–1067.

Chun, K., and Wise, K. D. 1985. A high performance silicon tactile imager based on a capacitive cell. *IEEE Trans. on Elect. Devices* 32(7):1196–1201.

Fearing, R. S. 1984 (San Diego). Simplified grasping and manipulation with dextrous robot hands. *American Control Conference,* pp. 32–38.

Fearing, R. S. 1986 (San Francisco). Implementing a force strategy for object re-orientation. *IEEE Int. Conf. on Robotics and Automation,* pp. 96–102.

Fearing, R. S. 1987a (Raleigh, North Carolina). Some experiments with tactile sensing during grasping. *IEEE Int. Conf. on Robotics and Automation,* pp. 1637–1643.

Fearing, R. S. 1987b. Tactile sensing, perception, and shape interpretation. Ph.D. thesis, Department of Electrical Engineering, Stanford University.

Fearing, R. S., and Binford, T. O. 1988 (Philadelphia). Using a cylindrical tactile sensor for determining curvature. *IEEE Int. Conf. on Robotics and Automation,* pp. 765–771.

Fearing, R. S., and Hollerbach, J. M. 1985. Basic solid mechanics for tactile sensing. *Int. J. Robot. Res.* 4(3):40–54.

Gladwell, G. M. L. 1980. *Contact Problems in the Classical Theory of Elasticity.* Alphen aan den Rijn, Netherlands: Sijthoff and Nordhoff.

Hillis, W. D. 1981. Active touch sensing. S.M. thesis, Department of Electrical Engineering and Computer Science, MIT.

Jacobsen, S. C., McCammon, I. D., Biggers, K. B., and Phillips, R. P. 1988. Design of tactile sensing systems for dextrous manipulators. *IEEE Control Syst.* 8(1):3–13.

Johnson, K. L. 1985. *Contact Mechanics.* Cambridge, England: Cambridge University Press.

Oppenheim, A. V., and Schafer, R. W. 1975. *Digital Signal Processing.* Englewood Cliffs, N.J.: Prentice-Hall.

Phillips, J. R., and Johnson, K. O. 1981. Tactile spatial resolution III. A continuum mechanics model of skin predicting mechanoreceptor responses to bars, edges, and gratings. *J. Neurophysiol.* 46(6):1204–1225.

Pratt, W. K. 1978. *Digital Image Processing.* New York: John Wiley & Sons.

Siegel, D. M. 1986. Contact sensors for dextrous robotic hands. TR-900. Cambridge, Mass.: MIT Artificial Intelligence Laboratory.

Siegel, D. M., Garabieta, I., and Hollerbach, J. M. 1985 (Cambridge, Mass.). A capacitive based tactile sensor. *SPIE Conf. on Intelligent Robots and Computer Vision.*

Smith, J. O., and Liu, C. K. 1953. Stresses due to the tangential and normal loads on an elastic solid with application to some contact stress problems. *J. Applied Mechanics Trans. ASME* 75:157–166.

Speeter, T. H. 1987. Analysis and control of robotic manipulation. Ph.D. thesis, Department of Biomedical Engineering, Case Western Reserve University.

Thomas, G. B. 1968. *Calculus and Analytic Geometry.* Reading, Mass.: Addison-Wesley.

Timoshenko, S., and Goodier, J. N. 1951. *Theory of Elasticity.* New York: McGraw-Hill.